

Asymptotic Giant Branch models at very low metallicity

S. Cristallo^{1,*}, *L. Piersanti*¹, *O. Straniero*¹, *R. Gallino*², *I. Domínguez*³ and *F. Käppeler*⁴

¹ Osservatorio Astronomico di Teramo (INAF), via Maggini 64100 Teramo, Italy

² Dipartimento di Fisica Generale, Università di Torino, via P. Giuria 1, 10125 Torino, Italy

³ Departamento de Física Teórica y del Cosmos, Universidad de Granada, 18071 Granada, Spain

⁴ Forschungszentrum Karlsruhe, Institut für Kernphysik Postfach 3460, D-76021 Karlsruhe, Germany

* Email: cristallo@oa-teramo.inaf.it

Abstract: In this paper we present the evolution of a low mass model (initial mass $M=1.5 M_{\odot}$) with a very low metal content ($Z = 5 \times 10^{-5}$, equivalent to $[\text{Fe}/\text{H}] = -2.44$). We find that, at the beginning of the AGB phase, protons are ingested from the envelope in the underlying convective shell generated by the first fully developed thermal pulse. This peculiar phase is followed by a deep third dredge up episode, which carries to the surface the freshly synthesized ^{13}C , ^{14}N and ^7Li . A standard TP-AGB evolution, then, follows. During the proton ingestion phase, a very high neutron density is attained and the s-process is efficiently activated. We therefore adopt a nuclear network of about 700 isotopes, linked by more than 1200 reactions, and we couple it with the physical evolution of the model. We discuss in detail the evolution of the surface chemical composition, starting from the proton ingestion up to the end of the TP-AGB phase.

Keywords: stars: AGB and post-AGB — physical data and processes: nuclear reactions, nucleosynthesis, abundances

1 Introduction

The interpretation of the already available and still growing amount of data concerning very metal-poor stars (see Beers & Christlieb (2005) for the classification of these objects) require reliable stellar models. A significant fraction ($\sim 25\%$) of stars with $[\text{Fe}/\text{H}] < -2.5$ show carbon-enriched atmospheres (Carbon Enhanced Metal Poor stars - CEMP stars). Moreover, many CEMP stars ($\sim 75\%$) are characterized by s-process enhanced patterns (CEMP-s): in this paper we will only address to this sub-class of low metallicity stars. CEMP-s stars belong to the Galactic Halo and, therefore, are old (~ 14 Gyr) low mass ($M < 0.9 M_{\odot}$) objects; notwithstanding, they show the concomitant enhancements of C, N and s-process elements, which are commonly ascribed to the complex interplay of nucleosynthesis, mixing and mass loss taking place along the Asymptotic Giant Branch (AGB). When these low mass stars reach the AGB, their envelope is so small that third dredge up (TDU) may not take place, so they are probably dwarfs or giants belonging to binary systems. Therefore, the C-enhancement and the products of the neutron capture nucleosynthesis could result from an ancient accretion process (via stellar wind or, less likely, via Roche lobe overflow) from the (now extinct) AGB companion (see, e.g., Roederer et al. 2008; Thompson et al. 2008). Note that a recent determination of radial velocities for a sample of CEMP-s stars suggests that all of these objects are members of binary systems (Lucatello et al. 2005). Some of these stars present exotic chemical distributions and, for this

reason, represent the current frontier of AGB modeling.

At very low metallicities, there is a minimum mass (which increases with decreasing the metallicity) under which models suffer proton ingestion from the envelope down to the underlying convective He-intershell. This occurs during the first fully developed thermal pulse (TP). We refer to this episode as the Proton Ingestion Episode (PIE). Larger mass models follow a standard TP-AGB evolution. This feature has already been found by many authors (Hollowell et al. 1990; Fujimoto et al. 2000; Suda et al. 2004; Iwamoto et al. 2004; Straniero et al. 2004; Cristallo et al. 2007; Campbell & Latt 2008; Lau et al. 2009): the occurrence of PIE is therefore a robust prediction, in spite of the different physics adopted in the various works. Moreover, recent 3D hydrodynamical simulations (Woodward et al. 2008) confirm this peculiarity, which characterizes very metal-poor models. A full understanding of the involved physics is therefore mandatory.

In next Sections, we present and discuss the evolution of an AGB model with initial mass $M=1.5 M_{\odot}$ and $Z = 5 \times 10^{-5}$, with emphasis on the effects on the stellar structure caused by the PIE. The model has been computed with the FRANEC stellar evolutionary code (Chieffi et al. 1998); details of the mixing scheme (see next Section) and latest improvements to the code are described in Cristallo et al. (2009). We assume a solar-scaled initial distribution (Lodders 2003), although at low metallicities a clear oxygen enhancement has been observed by many authors (see, e.g., Abia & Rebolo 1989).

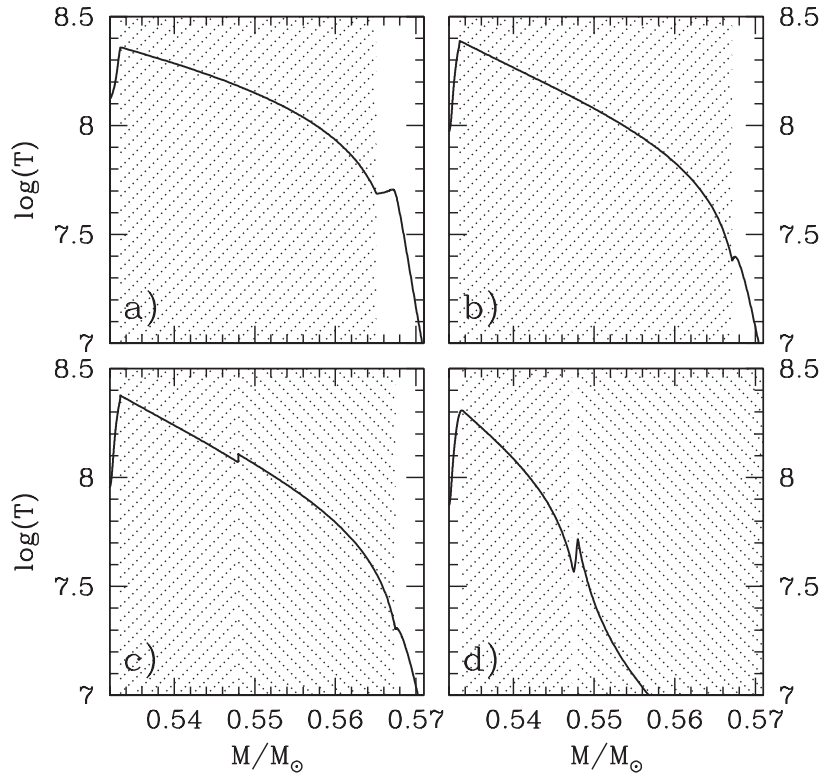


Figure 1: Evolution of the temperature within the He-intershell during the PIE. We plot the profiles at the beginning of proton ingestion (panel a, $\Delta t=0$ yr), soon before the convective shell splitting (panel b, $\Delta t=1.6457$ yr), soon after the convective shell splitting (panel c, $\Delta t=1.6468$ yr) and during the relaxing phase (panel d, $\Delta t=2.1843$ yr). Note how the convective shell (shaded region) in the top left panel is not yet fully developed. Different shading directions (panel c and d) indicate separate convective regions. See text for details.

2 The Proton Ingestion Episode

As outlined in the previous Section, at the beginning of the thermally pulsing phase of low mass metal-poor models, the convective shell powered by 3α reactions may extend up to the base of the H-rich envelope. This only occurs at low metallicities and is due to the flattening of the entropy peak characterizing the H-burning shell. At low Z , in order to compensate the reduction of CNO catalysts, the temperature of the H-shell increases and, consequently, the entropy within the H-shell decreases (entropy variation is defined as $dS = dQ/T$, where dQ is the exchanged heat and T is the temperature). Therefore, while at larger metallicities mixing is prevented by the entropy peak of the H-shell (Iben 1977), at low metallicities protons can be mixed within the convective shell and captured by the abundant ^{12}C . The temperature profile within the convective shell runs from about $T = 5.0 \times 10^7$ K at the outer border to $T = 2.3 \times 10^8$ K at the bottom (see top left panel of Fig. 1). At such high temperatures H-burning is very efficient and, therefore, protons are

captured on-flight by CNO isotopes before reaching the bottom of the convective shell. In these conditions, we can distinguish three different regions within the flash-driven convective shell:

- the external zone, where the CNO-burning time scale (τ_{CNO}) is largely greater than the mixing time scale;
- the inner zone, where temperature is so high that the mixing efficiency is largely smaller than the burning one;
- an intermediate zone, where the nuclear and mixing time scales are comparable.

The best approach to this situation is the simultaneous solution of the differential equations describing the physical structure of a star, the nuclear burning and the mixing. However, it has to be noticed that this computational scheme can be used only with small nuclear network, while it can not be applied when using very large network, including several hundreds of isotopes and nuclear processes. For this reason, in our simulations we adopt a different approach. We fully couple the structure equations with those describing the nuclear burning, so that we directly take into account the energetic feedback of nuclear reactions on the

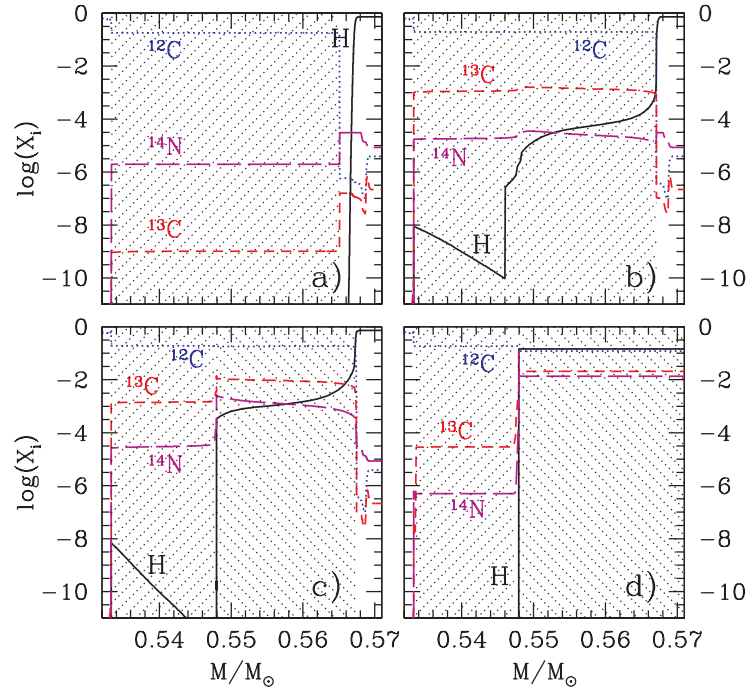


Figure 2: Evolution of selected key isotopes within the He-intershell during the PIE.

physical properties of the model (mainly the temperature profile). Moreover, this allows us to determine accurately the temperature gradient and, thus, the location and the mass extension of the zones unstable for convection. Hence, convection-induced mixing is computed by adopting the time dependent formalism described in Chieffi et al. (2001), where the mixing efficiency depends linearly on the temporal time step Δt of the model. In our simulation, during the PIE, we limit Δt to 50% of the mixing turnover time scale for the whole convective shell (τ_{mix}), in order to avoid the unrealistic fully homogenization of that region. All the chemical species are mixed within the whole unstable zone, with the exception of protons, which are mixed from the outer border of the convective shell down to the mass coordinate M_P , where $\tau_{CNO} = f\Delta t$, $f < 1$ being a free parameter. According to our choice on Δt , at M_P τ_{CNO} results definitively smaller than τ_{mix} (at least by a factor of $2/f$): this implies that protons consumption via nuclear burning is much more rapid than the supply via the convection-driven mixing. As a consequence, in nature below this point it is hardly unlikely for protons to survive. In the computation of PIE, we fix $f = 1/3$ (this implies that at M_P the temperature roughly corresponds to $T \sim 1.3 \times 10^8$). Such a choice is based on a series of evolutionary sequences computed with different values of f . Our results show that for $f > 1/3$ protons are accumulated in cool zones where H-burning is inefficient, while for $f < 1/3$ protons are mixed down to zones inconsistent with the on-flight burning.

In panel a of Fig. 2 we report the abundances of H, ^{12}C , ^{13}C and ^{14}N at the beginning of proton ingestion.

Note the large ^{12}C abundance, due to the partial He-burning inside the convective shell via 3α reactions, and the relatively low abundances of ^{13}C and ^{14}N , which result from the dilution, within the convective shell, of the ashes left by the H-burning shell during the previous interpulse phase. Similarly, in panel a of Fig. 3 we plot the contributions to energetics generated by proton captures (blue long-dashed curve) and by α captures (dark solid curve). Two peaks clearly emerge from the figure: the most internal one is due to 3α reactions (which power convection within the He-intershell) while the second peak (more external and shallow) comes from the CNO cycle in the H-burning shell. We plot apart the contribution of the $^{13}\text{C}(\alpha, n)^{16}\text{O}$ reactions, in which we also consider the energy release by the related neutron captures (short-dashed red curve).

Upper right panels (panels b) of Figures 1, 2 and 3 depict the situation 1.6457 yr after the beginning of protons ingestion. Protons are captured by the abundant ^{12}C , leading to the nucleosynthesis of ^{13}C and ^{14}N . Due to the concomitant actions of mixing and burning, the resulting abundances strongly differ with respect to the ones of the radiative H-burning shell, in which a full CNO equilibrium is attained and the most abundant synthesized isotope is ^{14}N . During the PIE, the H-burning is instead always out of equilibrium and this translates in a large production of ^{13}C and, at a lower level, of ^{14}N , while ^{16}O remains practically untouched. Technically, this is due to the fact that isotopes cannot locally pile up (and then reach the equilibrium value) due to the presence of convective motions. Note that ^{13}C and ^{14}N are correctly

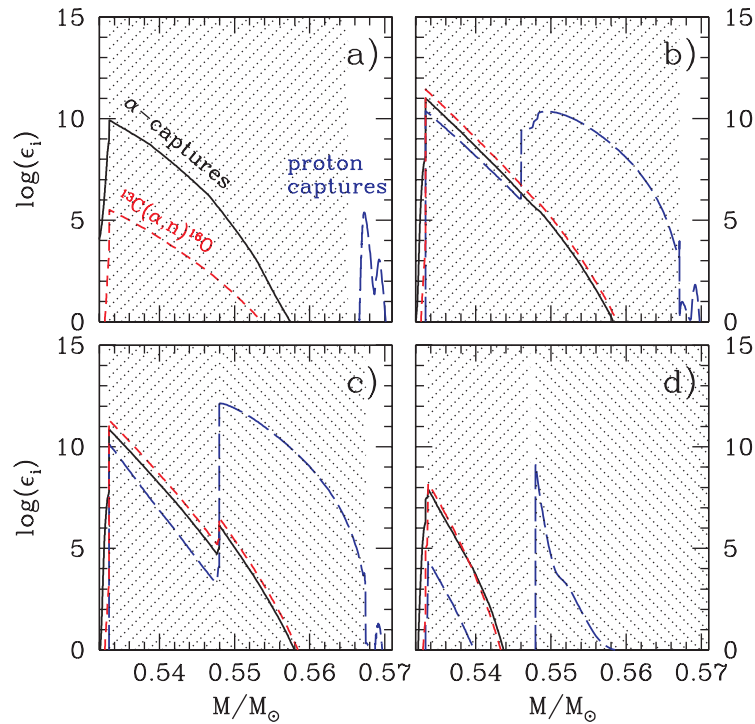


Figure 3: Evolution of different contributions to energetics within the He-intershell during the PIE.

mixed down to the base of the convective shell, because their burning timescales are always lower than the model temporal step. The hydrogen profile extends down to $M \sim 0.548 M_{\odot}$. The very small H abundance under this limit basically derives from $^{14}\text{N}(n,p)^{14}\text{C}$ reactions: neutrons mainly come from the $^{13}\text{C}(\alpha,n)^{16}\text{O}$ reaction, which is very efficiently activated at the bottom of the convective shell. This is clearly shown in panel **b** of Fig. 3, in which emerges that $^{13}\text{C}(\alpha,n)^{16}\text{O}$ reactions (and related neutron captures) represent the major energy source at the bottom of the convective shell. At the same time, the contribution of CNO burning boosts a second energy peak, whose mass coordinate is determined by the maximum penetration of protons within the convective shell. When the maximum CNO energy peak slightly exceeds the value of the He-burning peak, an inversion in the temperature profile occurs (see panel **c** of Fig. 1) and the convective shell splits into two sub-shells: the lower one boosted by the $^{13}\text{C}(\alpha,n)^{16}\text{O}$ reactions and the upper one by the CNO cycle. After the splitting event, the two convective shells follow separate evolutions.

In the lower shell, the $^{13}\text{C}(\alpha,n)^{16}\text{O}$ reaction consumes the available ^{13}C and produces a very large neutron flux. At the bottom of the shell, a neutron density as large as $n_n \sim 10^{15} \text{ cm}^{-3}$ is attained, allowing the synthesis of isotopes by-passed by a standard s-process. Since so high a neutron density moves the nucleosynthetic path away from the β stability valley, we extended the nuclear network with respect to that one used in previous works: the number of isotopes is increased from 500 to about 700 and the number of nu-

clear reactions grows from 700 to about 1200.

In the upper shell, the ^{13}C and the ^{14}N continue to increase thanks to the burning of freshly ingested protons from the external layers. In this phase, the CNO cycle is the major energy source in the star (see panel **c** of Fig. 3). Then, the structure starts expanding, causing the temperature of the whole region to rapidly decrease (see panel **d** of Fig. 1). During this phase, both the energy sources boosting the two shells quench off (see panel **d** of Fig. 3); in the meanwhile, the upper shell extends in mass.

Later on, the envelope completely engulfs the upper shell, dredging up to the surface a large amount of ^{13}C and ^{14}N . The lower shell, thanks to the steep pressure and density gradients formed in the splitting region, remains part of the He-intershell region and the isotopes synthesized in this region are later diluted in the following TP. Owing to the increase of the CN abundance in the envelope, the further evolution of this models resembles that of a standard AGB, preventing the occurrence of further PIEs. In the upper panel of Fig. 4 we report the temporal evolution of the mass coordinates of (top to bottom): the inner border of the convective envelope, the maximum energy production of the H-burning shell and the maximum energy production within the H-depleted core. In the lower panel we plot the H-burning and He-burning contributions to luminosity. Note the H-burning burst ($L_{\text{H}} > 10^9 L_{\odot}$) caused by the PIE. This model undergoes 25 additional TDU episodes, each one followed by the formation of a ^{13}C pocket (Straniero et al. 2006; Cristallo et al. 2009), which radiatively burns during the interpulse

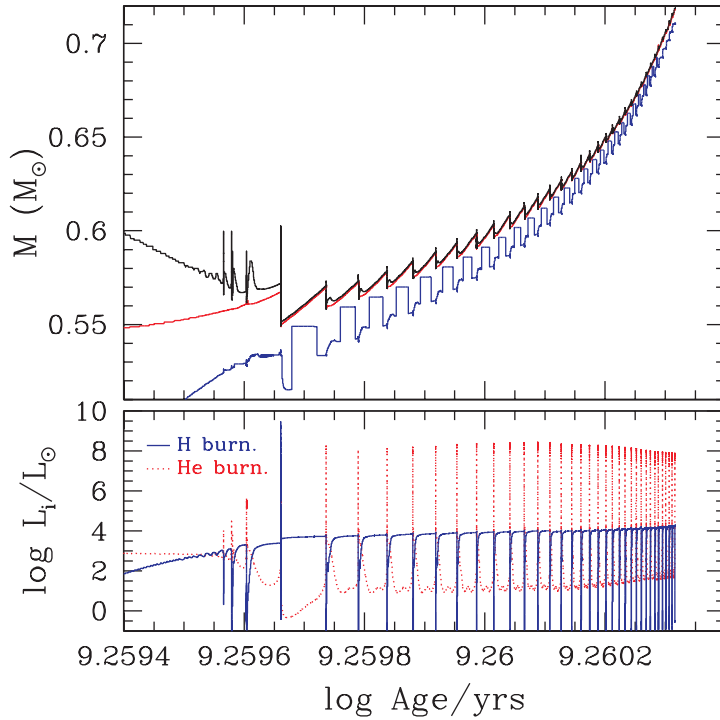


Figure 4: Upper panel: temporal evolution of the mass coordinates of (top to bottom) the inner border of the convective envelope, the maximum energy production of the H-burning shell and the maximum energy production within the H-depleted core. Note the occurrence of a deep TDU (hereafter d-TDU) at the beginning of the TP-AGB phase, as a consequence of proton ingestion. Lower panel: temporal evolution of the H-burning and He-burning contributions to luminosity.

period. The final surface composition is therefore a combination of two different nucleosynthetic channels: the first being a consequence of the PIE and the second coming from the s-process in the radiative ^{13}C pockets.

3 Nucleosynthesis Results

In Fig. 5 we report the evolution of selected heavy isotopes during the PIE: ^{89}Y (representative of light, ls, s-process elements), ^{139}La (representative of heavy, hs, s-process elements) and ^{208}Pb (which is strongly produced by the s-process in metal-poor stars). Tracing s-process elements have been selected basing on Busso et al. (2001). During the first phases of proton ingestion (see panel **a** of Fig. 5), the ^{13}C abundance (about 10^{-9} in mass fraction) does not allow an appreciable s-process production: heavy elements abundances are therefore the initial ones (in the previous phases of the stellar evolution no neutron sources have been in fact efficiently activated). During the following phase, up to the splitting event, we obtain a non negligible production of heavy elements, with particular efficiency in the production of hs elements (see panel **b** of Fig. 5). Once the splitting has occurred, the nucleosynthesis in the two shells follow completely different behaviors. In the lower shell, where ^{13}C is destroyed

at high temperatures ($T_{max} = 2.5 \times 10^8$ K), lead and hs elements are produced. In the upper shell, instead, ^{13}C burns at lower temperatures ($T_{max} \leq 10^8$ K, see panel **c** and **d** in Fig.1) and it is continuously added by the active proton burning. The final effect is a net production of ls elements only (see panel **d** in Fig. 5). When the envelope dredges up the isotopes synthesized in the upper shell, the surface distribution of the model is therefore enriched in ls elements, showing hs and lead abundances close to the initial ones (blue dotted curve in Fig. 6). The mass dredged up during the d-TDU is $\Delta M_{\text{TDU}} \sim 1.7 \times 10^{-2} M_{\odot}$; the corresponding efficiency (defined by means of the λ factor¹) is 2.7. After the d-TDU episode, the model follows a standard evolution. The isotopes synthesized in the lower shell are diluted in the convective shell generated by the following TP and their signature appears at the surface after the second TDU episode (red short-dashed curve in Fig. 6). The surface s-process distribution after the 2nd TDU mimics the expected distribution of models at low metallicity (Bisterzo et al. 2008), characterized by a growing sequence ls-hs-lead. Such a trend is even more strong as the number of TPs grows, displaying a final distribution character-

¹ λ is defined as the ratio between the mass of the H-depleted material that is dredged up and the mass of the material that has been burned by the H-shell during the previous interpulse period.

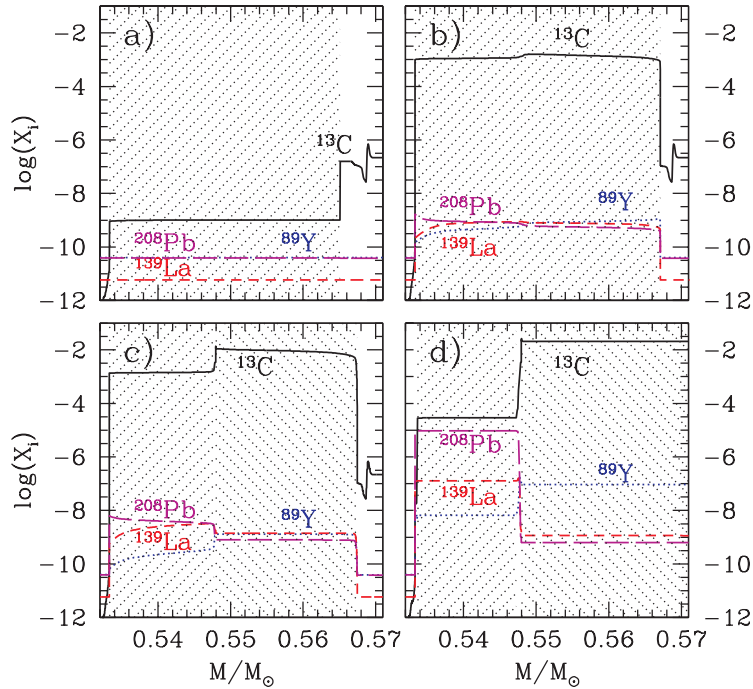


Figure 5: Temporal evolution of selected heavy isotopes during the PIE.

ized by $[\text{ls}/\text{Fe}]=2.02$, $[\text{hs}/\text{Fe}]=2.55$ and $[\text{Pb}/\text{Fe}]=3.50$ (dark solid curve in Fig. 6). In the plotted final distribution we took into account the decays of radioactive isotopes (as, for example, the β decay of long-lived ^{93}Zr to ^{93}Nb) and, therefore, this distribution can be compared with observational data of extrinsic AGBs.

3.1 Light elements

As outlined in Section 2, a huge N enhancement results as a consequence of proton ingestion from the top of the convective shell, a possibility early recognized by Hollowell et al. (1990). After the d-TDU following the PIE, the surface is in fact enriched not only in ^{12}C (as in a standard TDU), but also in ^{13}C and ^{14}N . In Fig. 7 we plot the $[\text{C}/\text{N}]$ ratio as a function of $[\text{C}/\text{Fe}]$, while in Fig. 8 we report the logarithm of the $^{12}\text{C}/^{13}\text{C}$ isotopic ratio as a function of $[\text{C}/\text{Fe}]$. In order to highlight the effects of the PIE, we report the same ratios for a model with initial mass $M = 2 M_{\odot}$ and $Z = 1 \times 10^{-4}$ (Cristallo et al. 2009), which follows a standard AGB evolution. Moreover, we also display spectroscopic data of CEMP-s stars (both Giants and MS Stars) extracted from the SAGA database (Suda et al. 2008): our selecting criteria have been metallicity ($-2.9 < [\text{Fe}/\text{H}] < -2.2$), a consistent s-elements enhancement ($[\text{Ba}/\text{Fe}] > 1.0$) and data completeness (values of C, N and $^{12}\text{C}/^{13}\text{C}$ collected from single surveys). The final $[\text{C}/\text{N}]$ ratio attained by our $1.5 M_{\odot}$ model better agrees with observational data of CEMP-s stars, which show values ranging between 0 and 1.3. For the sake of clarity, observational data show lower $[\text{C}/\text{Fe}]$ ratios with re-

spect to our model, but since the majority of these stars belong to binary systems (Lucatello et al. 2005), a dilution factor has to possibly be accounted for (depending on the masses and the geometry of the system) (Aoki et al. 2008; Thompson et al. 2008). Moreover, other physical mechanisms, such as gravitational settling, thermohaline mixing and the occurrence of the First Dredge Up, eventually led to a further dilution (Stancliffe & Glebbeek (2008) and references therein). Most of CEMP-s stars also show very low $^{12}\text{C}/^{13}\text{C}$ ratios (for some of them even close to the equilibrium value), therefore proving that the material within their envelopes experienced some H-burning. Our final value (~ 80) is strongly reduced with respect to models without the PIE (in which the $^{12}\text{C}/^{13}\text{C}$ ratio is larger than 10000) and, therefore, at low metallicities PIE help explaining the low observed carbon isotopic ratios. Observational data reported in Fig. 8 confirm this trend. Note that masses lower than $1.5 M_{\odot}$ experience fewer TDU episodes and, therefore, lower final $^{12}\text{C}/^{13}\text{C}$ are expected with respect to the model presented in this paper (Cristallo et al., in preparation). Moreover, we remember that large enough masses (the exact value depending on the metallicity) experience the Hot Bottom Burning (HBB) (Sugimoto 1971), showing therefore ^{13}C and ^{14}N enriched surfaces. However, the PIE can not occur at metallicities larger than $[\text{Fe}/\text{H}] > -2$ (Cristallo et al. 2007) and the mass experiencing HBB grows when increasing the metallicity. Additional extra-mixing mechanism, working during both the RGB and the AGB phase, are therefore requested to reproduce the low $^{12}\text{C}/^{13}\text{C}$ ratios detected in stars of intermediate metallicity (see Lebzelter et al.

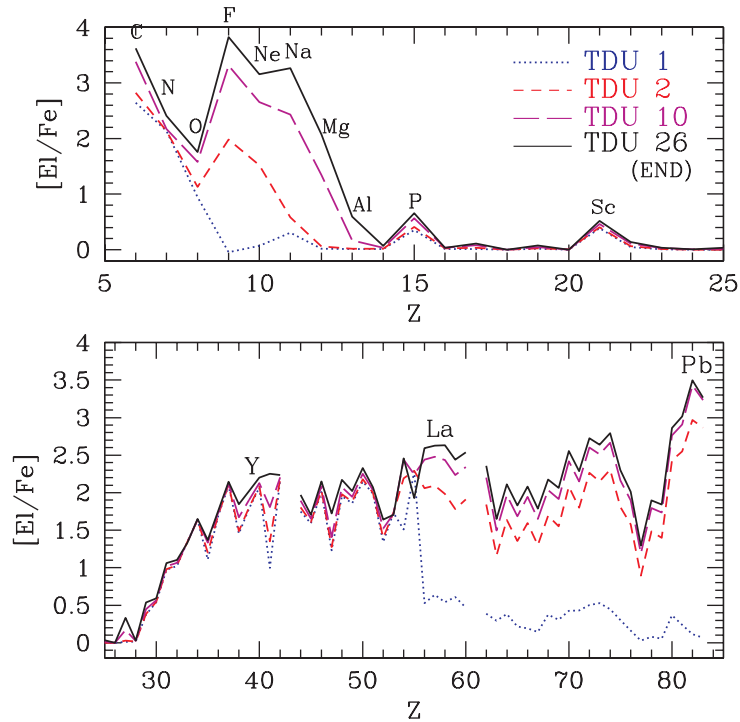


Figure 6: Surface abundances (in spectroscopic notation) of a model with initial mass $M=1.5 M_{\odot}$ model and $Z = 5 \times 10^{-5}$ after selected TDU episodes. Gaps at $Z = 43$ and $Z = 61$ correspond to unstable elements, Tc and Pm, respectively.

2008) as well in Galactic Open and Globular Clusters (see, e.g., Gratton et al. 2000).

Finally, let us discuss a further interesting feature, already noted by Iwamoto et al. (2004), marking the PIE: a very large production of ${}^7\text{Li}$. We obtain a final $\log(\epsilon(\text{Li})) = 3.74$, about two order of magnitude higher than the lithium plateau observed at low metallicity (Spite & Spite 1982). The ${}^7\text{Li}$ production mechanism is very simple: during proton ingestion, ${}^3\text{He}$ nuclei are ingested within the convective shell (note that the envelope presents a quite large ${}^3\text{He}$ abundance, $X({}^3\text{He}) \sim 3 \times 10^{-4}$, due to the occurrence of the First Dredge Up). During the PIE, ${}^3\text{He}$ is rapidly captured by the abundant ${}^4\text{He}$, leading to the synthesis of ${}^7\text{Be}$. This isotope then captures an electron and synthesizes ${}^7\text{Li}$. At high temperatures, lithium has a very large cross section against proton captures and, if created in an hot environment, is rapidly destroyed. However, given the rapidity of the stellar evolution after the splitting event, the freshly synthesized beryllium has not enough time to capture electrons in a hot environment and, therefore, is rapidly diluted in the envelope by the d-TDU.

4 Conclusions

In this contribution we present the evolution of a low mass model ($M=1.5 M_{\odot}$) of very-low metallicity ($Z = 5 \times 10^{-5}$). We discussed in details the effect that proton

ingestion has on the physical stellar structure and on the following nucleosynthesis. As a by-product of the PIE, we found a large production of ${}^{13}\text{C}$, ${}^{14}\text{N}$ and ${}^7\text{Li}$. Moreover, we discussed the surface s-process distributions after the deep TDU following the PIE and after the standard TDU episodes. We are now exploring the effects of the Proton Ingestion Episode on models with different masses ($0.85 \leq M/M_{\odot} \leq 2.0$) and $Z = 5 \times 10^{-5}$ (Cristallo et al., in preparation). Proton ingestion occurs in all these models. While in the 1.5 and 2.0 M_{\odot} mass models the effects of proton ingestion on the final surface compositions are integrated by the occurrence of standard TDU episodes (as shown in this contribution), lower masses (0.85 and 1.0 M_{\odot}) show peculiar final surface compositions, determined by the PIE only. Note that PIE remarkably lowers the minimum mass for the occurrence of TDU.

5 Acknowledgments

S.C., O.S. and R.G. are supported by the Italian MIUR-PRIN 2006 Project ‘‘Final Phases of Stellar Evolution, Nucleosynthesis in Supernovae, AGB stars, Planetary Nebulae’’. The authors thank the anonymous referee, whose suggestions greatly improved the quality of this paper.

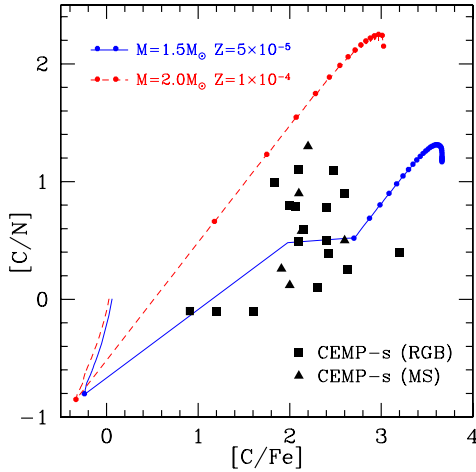


Figure 7: $[C/N]$ ratio as a function of $[C/Fe]$ for the $M = 1.5 M_{\odot}$ model with $Z = 5 \times 10^{-5}$. We also report a model with $M = 2.0 M_{\odot}$ and $Z = 1 \times 10^{-4}$. As a comparison, we plot spectroscopic data of Giant and MS CEMP-s stars. See text for details.

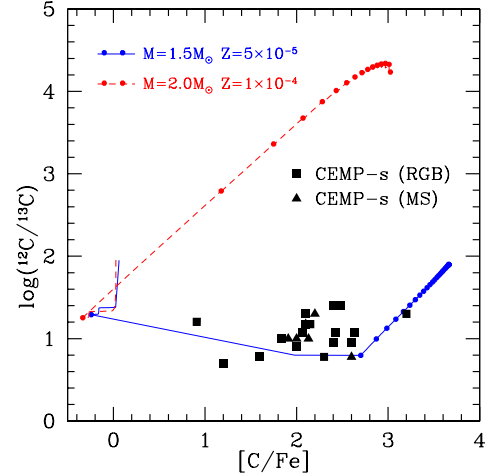


Figure 8: $^{12}C/^{13}C$ isotopic ratio as a function of $[C/Fe]$ for the $M = 1.5 M_{\odot}$ model with $Z = 5 \times 10^{-5}$. We also report a model with $M = 2.0 M_{\odot}$ and $Z = 1 \times 10^{-4}$. As a comparison, we plot spectroscopic data of Giant and MS CEMP-s stars. See text for details.

References

- Abia, C., & Rebolo, R., 1989, *ApJ*, 347, 186
- Aoki, W., et al., 2008, *ApJ*, 678, 1351
- Beers, T., & Christlieb, N., 2005, *ARA&A*, 43, 531
- Bisterzo, S., et al., 2008, *PASA*, in press
- Busso, M., Gallino, R., Lambert, D.L., Travaglio, C., Smith, V.V., 2001, *ApJ*, 557, 802
- Campbell, S.W., & Lattanzio, J.C., 2008, *A&A*, 490, 769
- Chieffi, A., Limongi, M., & Straniero, O., 1998, *ApJ*, 502, 737
- Chieffi, A., Domínguez, I., Limongi, M., & Straniero, O., 2001, *ApJ*, 554, 1159
- Cristallo, S., Straniero, O., Lederer, M.T., Aringer, B., 2007, *ApJ*, 667, 489
- Cristallo, S., Straniero, O., Gallino, R., Piersanti, L., Domínguez, I., Lederer, M.T., 2009, *ApJ* accepted (arXiv:0902.0243)
- Gratton, R.G., Carretta, E., Matteucci, F., Sneden, C., 2000, *A&A*, 358, 671
- Fujimoto, M.Y., Ikeda, Y., & Iben, I.Jr., 2000, *ApJ*, 529, 25
- Hollowell, D., Iben, I.Jr., Fujimoto, M.Y., 1990, *ApJ*, 351, 245L
- Iben, I.Jr., 1977, *ApJ*, 217, 788
- Iwamoto, N., Kajino, T., Mathews, G.J., Fujimoto, M.Y., Aoki, W., 2004, *ApJ*, 602, 377
- Lau, H.B., Stancliffe R.J. & Tout, C.A. 2009, *MNRAS* accepted (arXiv:0903.2324)
- Lebzelter, T., Lederer, M.T., Cristallo, S., Hinkle, K.H., Straniero, O., Aringer, B., 2008, *A&A*, 486, 511
- Lodders, K., 2003, *ApJ*, 591, 1220
- Lucatello, S., Tsangarides, S., Beers, T.C., Carretta, E., Gratton, R.G., Ryan, S.G., 2005, 625, 825L
- Roederer, I.U., et al., 2008, *ApJ*, 679, 1549
- Straniero, O., Cristallo, S., Gallino, R., Domínguez, I., 2004, *Mem.Soc.Astron.It.*, 75, 665
- Straniero, O., Gallino, R., Cristallo, S., 2006, *Nucl.Phys.A*, 777, 311
- Spite, M., & Spite, F., 1982, *A&A*, 115, 357
- Stancliffe, R.J., & Glebbeek, E., 2008, *MNRAS*, 389, 1828
- Suda, T., Aikawa, M., Machida, M.N., Fujimoto, M.Y., Iben, I.Jr., 2004, *ApJ*, 611, 476
- Suda, T., et al., 2008, *PASJ*, 60, 1159
- Sugimoto, D., 1971, *Prog. Theor. Phys.*, 45, 761
- Thompson, I.B., et al., 2008, *ApJ*, 677, 556
- Woodward, P., Herwig, F., Porter, D., Fuchs, T., Nowatzki, A., Pignatari, M., 2008, *AIPC*, 990, 300